

# A Bridgeless Boost Rectifier for Low-Voltage Energy Harvesting Applications

Haoyu Wang, *Student Member, IEEE*, Yichao Tang, *Student Member, IEEE*,  
and Alireza Khaligh, *Senior Member, IEEE*

**Abstract**—In this paper, a single-stage ac–dc power electronic converter is proposed to efficiently manage the energy harvested from electromagnetic microscale and mesoscale generators with low-voltage outputs. The proposed topology combines a boost converter and a buck-boost converter to condition the positive and negative half portions of the input ac voltage, respectively. Only one inductor and capacitor are used in both circuitries to reduce the size of the converter. A  $2\text{ cm} \times 2\text{ cm}$ , 3.34-g prototype has been designed and tested at 50-kHz switching frequency, which demonstrate 71% efficiency at 54.5 mW. The input ac voltage with 0.4-V amplitude is rectified and stepped up to 3.3-V dc. Detailed design guidelines are provided with the purpose of minimizing the size, weight, and power losses. The theoretical analyses are validated by the experiment results.

**Index Terms**—AC/DC conversion, boost, bridgeless, buck-boost, energy harvesting, low-voltage rectification.

## I. INTRODUCTION

**K**INETIC energy harvesters convert mechanical energy present in the environment into electrical energy. The past decade has seen an increasing focus in the research community on kinetic energy harvesting devices [1]. Typically, kinetic energy is converted into electrical energy using electromagnetic, piezoelectric, or electrostatic transduction mechanisms [2]. In comparison to electrostatic and piezoelectric transducers, electromagnetic transducers outperform in terms of efficiency and power density [3]. In this study, electromagnetic energy harvesters are considered for further study.

A general diagram of an electromagnetic generator is demonstrated in Fig. 1, where  $k$  is spring stiffness constant;  $m$  is the proof-mass;  $D_E$  and  $D_P$  represent electrical and parasitic dampers, respectively. Essentially, the energy harvesting system consists of a spring, a proof mass, and an electrical damper [4], [5]. The extrinsic vibrations excite the internal oscillation between the proof mass (magnet) and electrical damper (coils). The internal oscillation produces a periodically variable

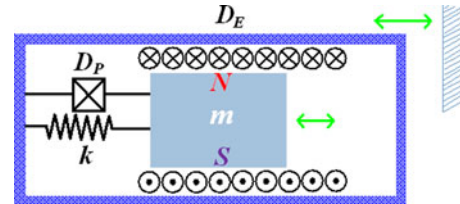


Fig. 1. General diagram of an electromagnetic microgenerator.

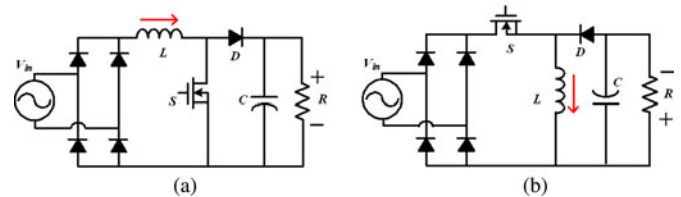


Fig. 2. Conventional two-stage diode-bridge ac–dc converters. (a) Boost rectifier. (b) Buck-boost rectifier.

magnetic flux in the coil, which induces a corresponding alternating output voltage.

In energy harvesting systems, power electronic circuit forms the key interface between transducer and electronic load, which might include a battery [6]. The electrical and physical characteristics of the power conditioning interfaces determine the functionality, efficiency, and the size of the integrated systems [7]. The power electronic circuits are employed to 1) regulate the power delivered to the load, and 2) actively manage the electrical damping of the transducers so that maximum power could be transferred to the load [8], [9]. The output voltage level of the microscale and mesoscale energy harvesting devices is usually in the order of a few hundred millivolts depending on the topology of device [10], [11]. The output ac voltage should be rectified, boosted, and regulated by power converters to fulfill the voltage requirement of the loads. Nonetheless, miniature energy harvesting systems have rigid requirement on the size and weight of power electronic interfaces.

Conventional ac–dc converters for energy harvesting and conditioning usually consists of two stages [12]–[14]. A diode bridge rectifier typically forms the first stage, while the second stage is a dc–dc converter to regulate the rectified ac voltage to a dc voltage (see Fig. 2). However, the diode bridge would incur considerable voltage drop, making the low-voltage rectification infeasible.

To overcome these drawbacks, CMOS diodes with low-voltage drops are investigated in the bridge rectifiers, to substitute conventional p–n junction diodes. Such reported

Manuscript received October 30, 2012; revised December 11, 2012 and January 15, 2013; accepted January 18, 2013. Date of current version May 3, 2013. Recommended for publication by Associate Editor F. Costa.

The authors are with the Power Electronics, Energy Harvesting and Renewable Energies Laboratory, Department of Electrical and Computer Engineering and the Institute for Systems Research, University of Maryland, College Park, MD 20742 USA (e-mail: wanghy@umd.edu; ychtang@umd.edu; khaligh@ece.umd.edu).

Color versions of one or more of the figures in this paper are available online at <http://ieeexplore.ieee.org>.

Digital Object Identifier 10.1109/TPEL.2013.2242903

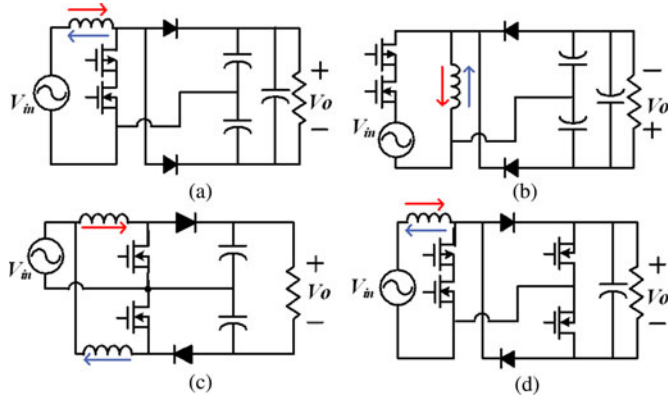


Fig. 3. Bridgeless ac-dc converters [6]. (a) Split capacitor boost converter. (b) Split capacitor buck-boost converter. (c) Dual polarity boost converter. (d) Boost converter with secondary switches.

diodes include 1) diode-connected passive MOSFET, which adopts threshold voltage cancellation techniques [15], [16], and 2) MOSFET, which is actively controlled by a comparator [6], [17]–[21]. In either case, the low-voltage-drop diode techniques require either additional bias networks or external comparators. Thus, both the complexity and the power loss of the circuitry would increase. Some converters reported in the literature use transformers as the first stage boosters to overcome the voltage drop in semiconductor devices [22], [23]. However, the size of the transformer could be unacceptably large in low-frequency energy harvesting applications.

Another approach to maximize the conversion efficiency in low-voltage rectification is to use bridgeless direct ac-dc converters [24]. Those topologies either use bidirectional switches and split capacitors, or two parallel dc-dc converters to condition positive and negative input voltages separately. For the split-capacitor topologies [see Fig. 3(a)–(c)], due to the low operation frequency of specified microgenerators, the capacitors have to be large enough to suppress the voltage ripple under a desired level. The increased size and number of energy storage components make those topologies impractical due to the size limitation of energy harvesters. On the other hand, the split capacitors could be eliminated by using two synchronous MOSFETs [see Fig. 3(d)]. However, the additional switches would incur extra switch loss and driving circuit dissipations.

The boost converter is the common power conditioning interface due to its simple structure, voltage step-up capability, and high efficiency. The buck-boost converter has ability to step up the input voltage with a reverse polarity; hence, it is an appropriate candidate to condition the negative voltage cycle. Besides, the boost and buck-boost topologies could share the same inductor and capacitor to meet the miniature size and weight requirements.

A new bridgeless boost rectifier, shown in Fig. 4, which is a unique integration of boost and buck-boost converters, is proposed in this paper. When the input voltage is positive,  $S1$  is turned ON and  $D1$  is reverse biased, the circuitry operates in the boost mode. As soon as the input voltage becomes negative, the buck-boost mode starts with turning ON  $S2$  and reverse biasing  $D2$ . MOSFETs with bidirectional conduction capability

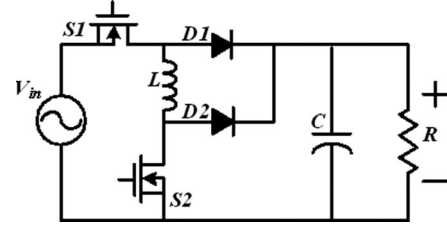


Fig. 4. Proposed bridgeless boost rectifier for low-voltage energy harvesting.

work as two-quadrant switches to ensure the circuitry functionality in both positive and negative voltage cycles. This topology was introduced in [25] for piezoelectric energy harvesting applications.

The circuit operation modes are described in Section II. In Section III, a detailed analysis of discontinuous conduction mode (DCM) is provided along with the averaged large signal modeling. The design procedures and guidelines are discussed in Section IV. Section V addresses the control schemes for DCM. Experiment results are reported to verify the previous theoretical analysis in Section VI. Section VII presents the conclusions.

## II. PRINCIPLE OF OPERATION

In electromagnetic energy harvesters, the internal oscillation between coils and magnet produces a periodically variable magnetic flux in the coil, which induces a corresponding output voltage. The power electronics interface (PEI) is employed to supply constant voltage and to deliver power to the load. In order to facilitate and simplify analyses, it is assumed that the input impedance of the PEI is significantly larger than the internal impedance of energy harvesting device. The induced voltage could be assumed to be a low amplitude sinusoidal ac voltage source. As the frequency of vibration source and induced voltage (usually less than 100 Hz) is much less in comparison to that of the switching frequency (around tens of kHz), the induced ac voltage can be assumed as a constant voltage source in each switching period. In this paper, a 0.4-V, 100-Hz sinusoidal ac voltage source is adopted to emulate the output of the electromagnetic energy harvester.

The DCM operating modes of the proposed boost rectifier are shown in Fig. 5. Each cycle of the input ac voltage can be divided into six operation modes. Modes I–III illustrate the circuit operation during positive input cycle, where  $S1$  is turned ON while  $D1$  is reverse biased. The converter operates as a boost circuit during Modes I–III, while switching  $S2$  and  $D2$ . The operation during negative input cycle is demonstrated in Modes IV–VI, where  $S2$  is turned ON while  $D2$  is reverse biased. In these modes, the converter operates similar to a buck-boost circuit.

**Mode I:** This mode begins when  $S2$  is turned ON at  $t_0$ . The inductor current is zero at  $t_0$ . The turn on of  $S2$  is achieved through zero current switching (ZCS) to reduce switching loss. Inductor  $L$  is energized by the input voltage as both  $S1$  and  $S2$  are conducting. Both diodes are reverse biased. The load is powered by the energy stored in the output filter capacitor  $C$ .

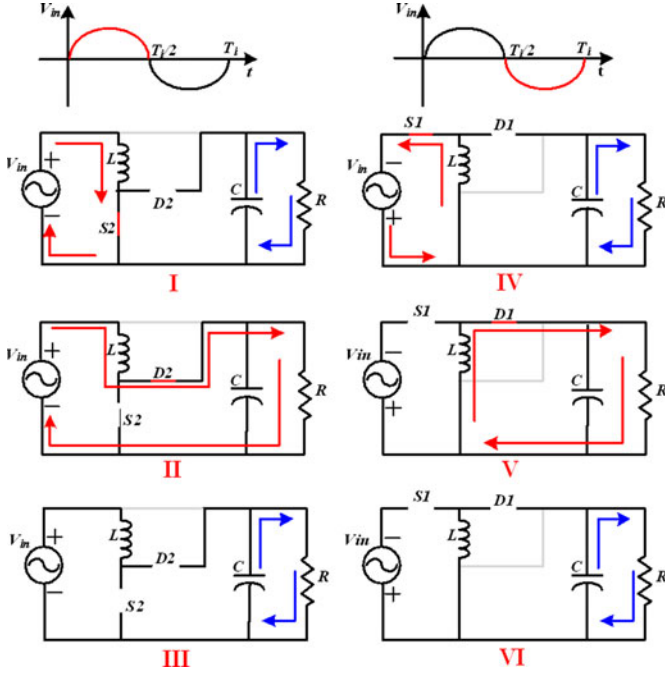


Fig. 5. Operating modes of the proposed boost rectifier.

**Mode II:**  $S2$  is turned OFF at  $t_1$ , where  $t_1 - t_0 = d_1 T_s$ ,  $d_1$  is the duty cycle of the boost operation, and  $T_s$  is the switching period. The energy stored in the inductor during Mode I is transferred to the load. The inductor current decreases linearly. During this mode, switching loss occurs during the turn on of diode  $D2$ .

**Mode III:**  $D2$  is automatically turned OFF as soon as the inductor current becomes zero at  $t_2$  ( $t_2 - t_1 = d_2 T_s$ ). This avoids the reverse recovery loss of diode. The load is again powered by the stored energy in the capacitor. The converter would return to Mode I as soon as  $S2$  is turned ON, if the input voltage is still in positive cycle.

**Mode IV:** During the negative input cycle, Mode IV starts as soon as  $S1$  is turned ON at  $t'_0$ . ZCS condition can also be achieved by ensuring the converter operation in DCM. The energy is transferred to the inductor  $L$  again, while the output filter capacitor  $C$  feeds the load.

**Mode V:** At  $t'_1$ ,  $S1$  is turned OFF, where  $t'_1 - t'_0 = d'_1 T_s$ ,  $d'_1$  is the duty cycle of the buck-boost operation. The energy stored in the inductor during Mode IV is transferred to the load. The inductor current decreases linearly. During this mode, switching loss occurs during the turn on of the diode  $D1$ .

**Mode VI:** When the inductor current decreases to zero at  $t'_2$  ( $t'_2 - t'_1 = d'_2 T_s$ ),  $D1$  is turned OFF at zero current. The load is continuously powered by the charge stored in the output capacitor. The converter would return to Mode IV as soon as  $S1$  is turned ON, if the input voltage is still negative.

According to the analyses of operation modes, the switches are turned ON with ZCS and the diodes are turned OFF with ZCS. Due to the DCM operation, the input current sensor can be eliminated and switching loss can be reduced. Moreover, the control scheme of DCM operation is relatively simpler. Since the circuit size can be reduced and the efficiency can be enhanced,

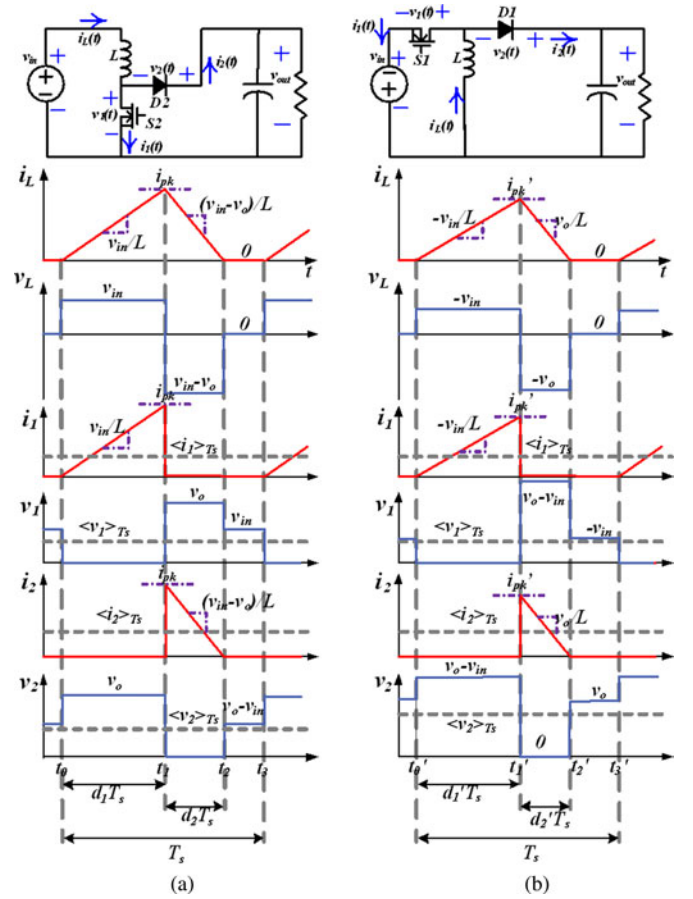


Fig. 6. Waveforms of the proposed boost/buck-boost rectifier. (a) Boost operation. (b) Buck-boost operation.

DCM operation is more suitable than continuous conduction mode (CCM) operation.

### III. THEORETICAL ANALYSIS AND MODELING

#### A. Large Signal Modeling

In order to analyze the steady-state operation of the proposed circuit, several assumptions are made during one switching cycle.

- 1) The output filter capacitor  $C$  is large enough to keep the output voltage  $V_o$  constant.
- 2) The input is a sinusoidal voltage source. The switching frequency is much higher than the input voltage frequency. During each switching cycle, the input voltage could be treated as a constant voltage source and be expressed as (1), where  $T_i$  is the period of input voltage

$$v_{in}(t) = V_m \sin(2\pi t/T_i). \quad (1)$$

- 3) Internal series resistances of passive components are not taken into account for convenience in calculations.

According to Fig. 6, during the boost operation cycle  $[t_0, t_3]$ , the average transistor voltage  $\langle v_1(t) \rangle_{T_s}$ , can be expressed as

$$\langle v_1(t) \rangle_{T_s} = (1 - d_1 - d_2) \langle v_{in}(t) \rangle_{T_s} + d_2 \langle v_o(t) \rangle_{T_s}. \quad (2)$$

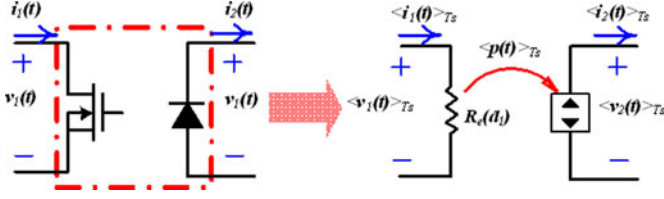


Fig. 7. Averaged switch model of general two-switch network in DCM.

The average switch current  $\langle i_1(t) \rangle_{T_s}$  is derived by integrating the  $i_1(t)$  waveform as depicted in Fig. 6(a) during one switching period

$$\langle i_1(t) \rangle_{T_s} = \frac{1}{T_s} \int_{t_0}^{t_3} i_1(t) dt = \frac{d_1^2 T_s \langle V_{in}(t) \rangle}{2L}. \quad (3)$$

The average diode voltage  $\langle v_2(t) \rangle_{T_s}$ , and the average diode current  $\langle i_2(t) \rangle_{T_s}$  can be expressed, respectively, as

$$\langle v_2(t) \rangle_{T_s} = d_1 \langle v_o(t) \rangle_{T_s} + (1 - d_1 - d_2) (\langle v_o(t) \rangle_{T_s} - \langle v_{in}(t) \rangle_{T_s}) \quad (4)$$

$$\langle i_2(t) \rangle_{T_s} = \frac{1}{T_s} \int_{t_0}^{t_3} i_2(t) dt = \frac{d_2^2 T_s (\langle v_{out}(t) \rangle - \langle v_{in}(t) \rangle)}{2L}. \quad (5)$$

According to the inductor volt-second balance,  $d_2(t)$  can be related to  $d_1(t)$  as

$$d_2 = d_1 \frac{\langle v_{in}(t) \rangle}{\langle v_o(t) \rangle - \langle v_{in}(t) \rangle}. \quad (6)$$

Using (2)–(6):

$$\frac{\langle v_1(t) \rangle_{T_s}}{\langle i_1(t) \rangle_{T_s}} = \frac{2L}{d_1^2 T_s} \quad (7)$$

$$\langle i_2(t) \rangle_{T_s} \langle v_2(t) \rangle_{T_s} = \frac{\langle v_1(t) \rangle_{T_s}^2}{2L / (d_1^2 T_s)}. \quad (8)$$

Similar derivations can also be applied to the buck-boost operation cycle  $[t'_0, t'_3]$ , and the same expressions can be derived.

According to (7), the average switch voltage  $\langle v_1(t) \rangle_{T_s}$  is proportional to the average switch current  $\langle i_1(t) \rangle_{T_s}$ . In other words, the switch behaves like an equivalent resistor with resistance  $R_e(d_1)$

$$R_e(d_1) = \frac{2L}{d_1^2 T_s}. \quad (9)$$

Inserting (9) into (8), the equivalent power out of the diode can be presented as

$$\langle p(t) \rangle_{T_s} = \langle i_2(t) \rangle_{T_s} \langle v_2(t) \rangle_{T_s} = \frac{\langle v_1(t) \rangle_{T_s}^2}{R_e}. \quad (10)$$

According to (10), the diode behaves like a controlled power source, the power of which is equals to the power consumption of the equivalent resistor  $R_e(d_1)$ . Thus, the switch network could be modeled by a loss-free resistor and a dependent power source, as illustrated in Fig. 7.

The equivalent circuit of the topology in the steady state can be modeled by replacing the switch network with its averaged model. In steady-state condition, in which the inductor and capacitor can be, respectively, replaced with short circuit

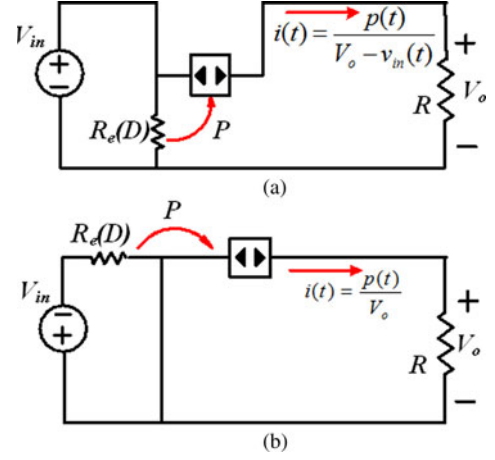


Fig. 8. DCM dc equivalent circuits representing (a) boost operation and (b) buck-boost operation.

and open circuit, the circuit can be simplified to the circuits of Fig. 8, where  $d_1(t) = D$ .

### B. Converter Analyses

In boost operation mode  $[0, T_i/2]$ , the instantaneous power delivered to the equivalent resistor in the model of Fig. 8(a) can be expressed as

$$p(t) = \frac{v_{in}^2(t)}{R_e} = \frac{V_m^2 \sin^2(2\pi t/T_i)}{R_e}. \quad (11)$$

The instantaneous current flowing through the load resistor  $R$  can be written as

$$i(t) = \frac{p(t)}{V_o - v_{in}(t)} = \frac{V_m^2 \sin^2(2\pi t/T_i)}{R_e [V_o - V_m \sin(2\pi t/T_i)]}. \quad (12)$$

Hence, the instantaneous power delivered to the load is

$$p_L(t) = V_o i(t) = \frac{V_o V_m^2 \sin^2(2\pi t/T_i)}{R_e [V_o - V_m \sin(2\pi t/T_i)]}. \quad (13)$$

For each boost cycle  $[0, T_i/2]$ , the total energy delivered to the load is obtained as

$$E_{in} = \int_0^{T_i/2} p_L(t) dt = \int_0^{T_i/2} \frac{V_o V_m^2 \sin^2(2\pi t/T_i)}{R_e [V_o - V_m \sin(2\pi t/T_i)]} dt. \quad (14)$$

On the other hand, the energy consumed by the load would be

$$E_o = \int_0^{T_i/2} p_o dt = \int_0^{T_i/2} \frac{V_o^2}{R} dt = \frac{V_o^2 T_i}{2R}. \quad (15)$$

According to the energy conservation principle, the energy delivered to the load is equal to the energy provided by the power supply. Using (9), (14), and (15)

$$\frac{V_o^2 T_i}{2R} = \frac{V_m^2 d_1^2 T_s}{4L} \int_0^{T_i/2} \frac{1 - \cos(4\pi t/T_i)}{[1 - V_m/V_o \sin(2\pi t/T_i)]} dt. \quad (16)$$

The integral part of (16) is a function of boost ratio  $(V_m/V_o)$ , which would be infinitely close to  $T_i/2$ , if the ratio is much larger than 1.



For low-voltage energy harvesting, the input voltage is usually smaller than 0.5 V. However, most of the electronic loads should be driven by a 3.3-V voltage. With the boost ratio larger than 6.6, the integral would become equal to  $T_i/2$ . Thus, (16) becomes

$$\frac{V_0^2 T_i}{2R} \approx \frac{V_m^2 d_1^2 T_s T_i}{8L}. \quad (17)$$

Similar equations can also be driven for the buck-boost operation ( $T_i/2$  to  $T_i$ ) according to the model provided in Fig. 8(b). Different from the boost operation, the power consumed by the loss-free resistor is all delivered to the load. The derivations lead to

$$\frac{V_0^2 T_i}{2R} = \frac{V_m^2 d_1^2 T_s T_i}{8L}. \quad (18)$$

Equations (16) and (18) reveal the essential relationship in the converter design, where (16) could be substituted by (17) as long as the boost ratio is much larger than unity.

#### IV. DESIGN PROCEDURE

If the voltage gain is much larger than unity, according to (17) and (18), the boost and buck-boost operations share the same duty cycle  $D$ , which is determined by the boost ratio ( $V_o/V_m$ ), the inductance of the inductor  $L$ , and the switching frequency  $f_s$ . Equation (19) defines the commutation relationship of the duty cycle of the proposed boost/buck-boost converter

$$D = d_1 = d'_1 = \frac{2V_o}{V_m} \sqrt{\frac{Lf_s}{R}}. \quad (19)$$

The boost ratio is defined according to the specific application, while the load resistance  $R$  is dependent on the output power level. With the specified power and voltage demands, the inductance is designed according to the desired range of duty cycle and switching frequency. The larger the switching frequency is, the smaller the inductance would be. In order to design a smaller inductor with purpose of obtaining smaller size and weight, a higher switching frequency is preferred. However, the higher the switching frequency is, the higher the switching loss would be. A tradeoff between the size of inductor and the switching loss should be taken into account in the design process.

Both the boost and buck-boost operations of the converter provide the same inductor current ripple, which can be expressed as

$$\Delta i_L = \frac{v_{in}(t)DT_s}{L}. \quad (20)$$

The maximum current ripple corresponds to the peak input voltage. According to previous analyses, the inductor, diodes, and MOSFETs share the same value of current ripple, which is defined in the following equation:

$$\Delta i_{L,\max} = \frac{V_m DT_s}{L}. \quad (21)$$

From (21), the current ratings of all those components could be found.

The voltage ratings of the MOSFETs and diodes are normally chosen higher than  $V_o$  with an appropriate margin for safe op-

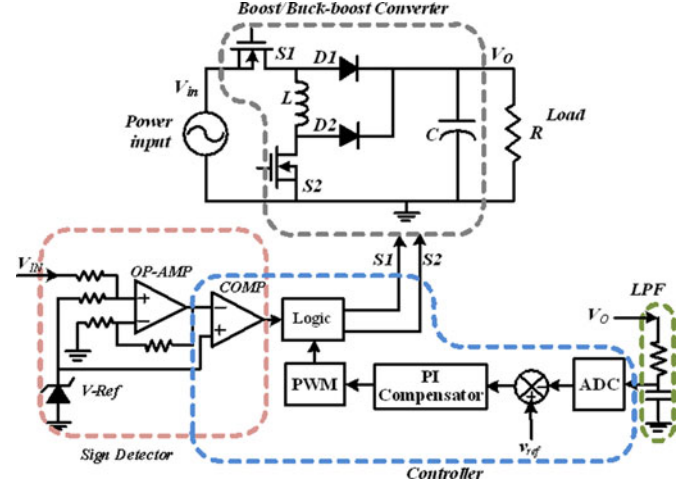


Fig. 9. Control circuit for the proposed converter.

eration. The turn-on resistances of MOSFETs and the forward voltage drop of diodes are the major components, which impact the efficiency.

#### V. CONTROL STRATEGY

For a dynamic EM energy harvester system, if the external excitation frequency is different from the intrinsic resonance frequency, the PEI should be able to match its input impedance with the internal impedance of the harvester so that maximum power point (MPP) could be tracked. This paper proposed a new topology, which has the maximum power point tracking (MPPT) capability. However, the main objective of this paper is to introduce the circuit topology, which is capable of satisfying the voltage requirement (3.3 V) of an electronic load. Thus, a voltage feedback control loop is utilized to regulate the load voltage.

The simplified scheme of the controller and power stage is illustrated in Fig. 9. The converter is designed to operate in DCM. The output voltage is filtered by a passive low-pass filter and then fed to the analog-to-digital converter (ADC) of the controller.

The difference between the ADC output and the desired voltage is calculated and compensated through the PI algorithm to generate an adjustable duty cycle signal. The switching signals of  $S1$  and  $S2$  are dependent on the polarity of the input voltage. A sign detector is used to determine the input voltage polarity. The Atmel Mega 16 A is selected as the controller in this paper, which has both on-chip analog comparator and integrated ADC and can be integrated with the sign detector.

The sign detector is composed of a voltage reference, an op-amp, and the on-chip analog comparator. The op-amp operates as an analog adder, where a dc bias (voltage reference) is added to the input voltage. The signal summation is compared with the voltage reference to detect the polarity.

#### VI. EXPERIMENT RESULTS AND LOSS ANALYSES

The printed circuit board (PCB) is designed to minimize the size of the prototype using surface-mount components with

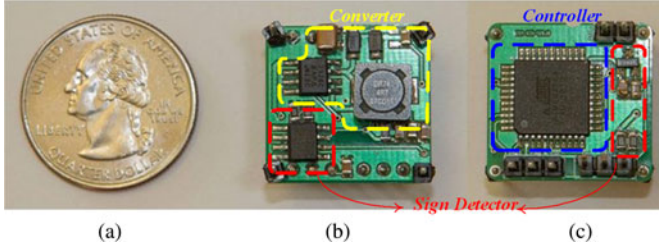


Fig. 10.  $2 \times 2 \text{ cm}^2$ , 3.34 g prototype of the proposed converter. (a) United States quarter. (b) Circuit Front. (c) Circuit Back.

TABLE I  
COMPONENTS AND PARAMETERS IN THE PROTOTYPE

COMPONENT	PARAMETERS	Part Number
$V_{in}$ (Input voltage)	0.4 V, 100 Hz	N/A
$V_o$ (output voltage)	3.3 V	N/A
Switching frequency	50 kHz	N/A
Power Inductor $L$	4.7 $\mu\text{H}$ , 3.34 A, 25.4 m $\Omega$	DR74-4R7-R
Filter Capacitor $C$	100 $\mu\text{F}$ , 6.3 V	C3225Y5V0J107Z
MOSFETs	20 V, 8 A, 22 m $\Omega$ @2.5 V	SI9926CDY
Schottky Diodes	20 V, 0.36 V@1 A	DFLS120L-7

lower packaging overhead. In the case of much lower power levels, it is possible to use components with least packaging overhead or in bare die form to further reduce the size and weight of the circuit. A highly compact power electronic interface prototype, depicted in Fig. 10, is fabricated. The prototype has a PCB size of  $2 \times 2 \text{ cm}^2$  and weighs 3.34 g. The component design details and electrical parameters are summarized in Table I.

$S2$  operates as the low-side switch with  $V_{GS2} = V_{G2}$ , while  $S1$  operates as the high-side switch with  $V_{GS1} = V_{G1} - V_{in}$ . In this case, due to small amplitude of input voltage, the minimum value of  $V_{GS1} = V_{G1} - V_M = 2.9 \text{ V}$  is still sufficient to turn on the  $S1$  with low conduction resistance. Thus, both  $S1$  and  $S2$  could be directly driven by the digital output of the controller.

The energy harvester is emulated by a signal generator cascaded with a high-pass filter, and a high current voltage follower (OPA548). The power source is programmed to have 0.4-V amplitude and 100-Hz frequency.

A milliwatt scale test is carried out in order to verify the theoretical analyses and simulations of the proposed topology. However, this proposed topology is not specifically limited to be used in milliwatt applications; it would also work in microwatt applications.

200- $\Omega$  resistive load is chosen to demonstrate the power transfer capability of the designed PEI prototype. With 200- $\Omega$  resistive load, the converter is capable of tightly regulating output voltage and delivering 54.5 mW to the load. Figs. 11–14 illustrate the experimental waveforms for the converter with a 200- $\Omega$  resistive load. Fig. 11 shows the waveforms of input voltage, gate signals of both switches, as well as the input current. During the positive input cycle,  $S1$  is turned ON, while  $S2$  is driven by the

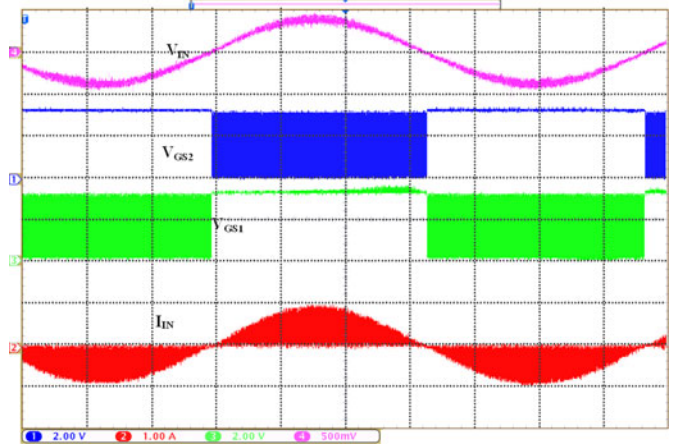


Fig. 11. From top to bottom: oscillograms of input voltage (0.5 V/div), boost gate pulse (2 V/div), buck-boost gate pulse (2 V/div), input current (1 A/div); time 4 ms/div,  $R = 200 \Omega$ .

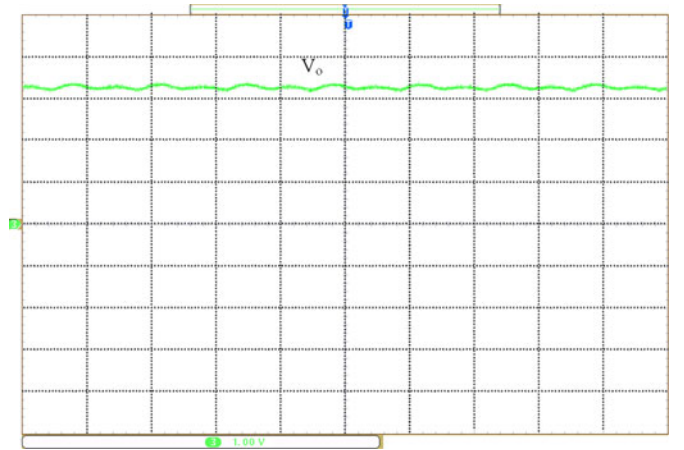


Fig. 12. Oscillogram of output voltage, 1 V/div; time 20 ms/div.  $R = 200 \Omega$ .

boost control scheme. When the circuit operates in the negative input cycle,  $S2$  is turned ON, while  $S1$  is controlled under the buck-boost conditioning strategy. As seen from Fig. 12, the output voltage is regulated at 3.3-V dc with approximately 0.2 V (i.e., 6%) voltage ripple.

Figs. 13 and 14 demonstrate the boost and buck-boost operations correspondingly. Closed-loop voltage control successfully stabilizes the duty cycle at 0.72 at the steady state. In boost operation, the input current increases with a rate of 33.3 mA/ $\mu\text{s}$ , and then drops fast with a rate of 200 mA/ $\mu\text{s}$ . The discontinuous condition lasts approximately 8  $\mu\text{s}$  during each cycle. In buck-boost operation, the input current becomes zero as soon as  $S1$  is switched OFF.

Figs. 15–17 show the experimental waveforms with 300- $\Omega$  resistive load while delivering 36.3-mW power. The steady-state duty cycled is 0.60 and the peak current is 0.84 A. Table II lists the comparisons between measured results from experiments and theoretical analyses. The measured duty cycles are slightly larger than theoretical derivation due to the fact that the analyses neglect the conduction and switching losses. The turn-on resistance of semiconductor devices and the series resistance of

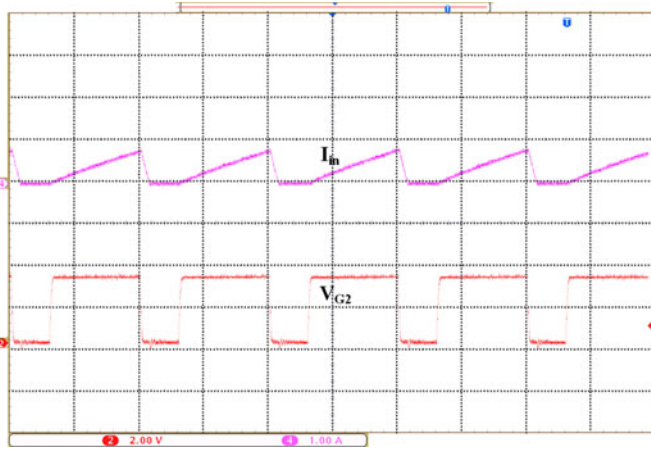


Fig. 13. From top to bottom: oscillograms of input current (500 mA/div), boost gate pulse (2 V/div); time 10  $\mu$ s/div.  $R = 200 \Omega$ .

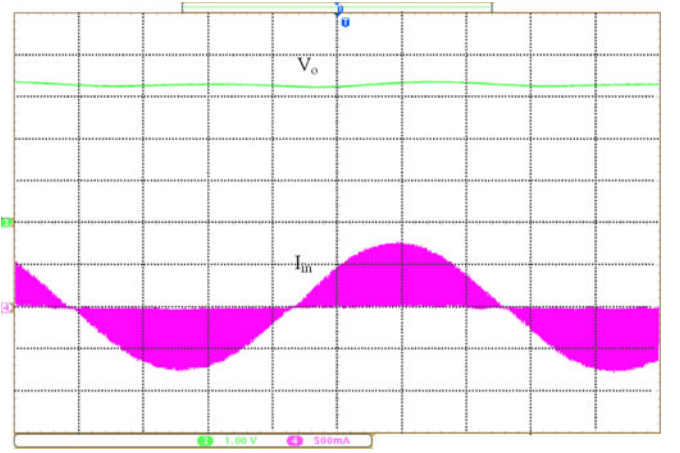


Fig. 15. From top to bottom: oscillograms of output voltage (1 V/div), input current (500 mA/div); time 4 ms/div,  $R = 300 \Omega$ .

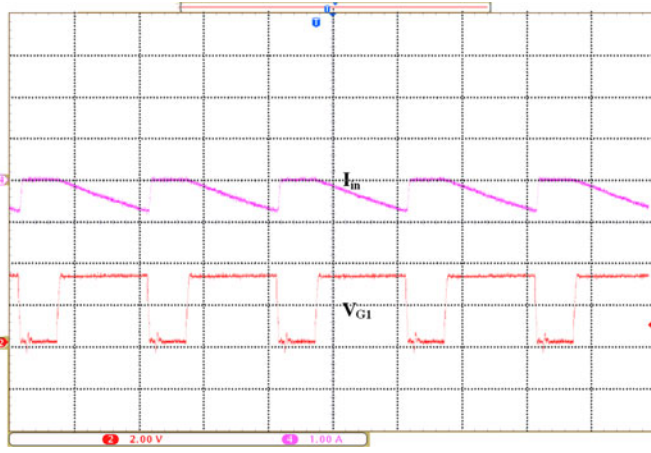


Fig. 14. From top to bottom: oscillograms of input current (500 mA/div), buck-boost gate pulse (2 V/div); time 10  $\mu$ s/div.  $R = 200 \Omega$ .

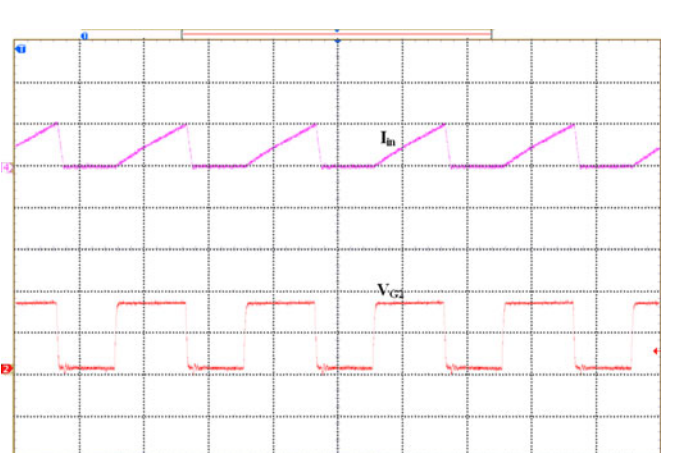


Fig. 16. From top to bottom: oscillograms of input current (1 A/div), boost gate pulse (2 V/div); time 10  $\mu$ s/div,  $R = 300 \Omega$ .

TABLE II  
COMPARISONS ON CALCULATED AND MEASURED PARAMETERS

Parameter	Calculated Value	Measured Value
Duty cycle ( $R = 200 \Omega$ )	0.65	0.72
$\Delta I_{in,max}$ ( $R = 200 \Omega$ )	1.1 A	1.02 A
Duty cycle ( $R = 300 \Omega$ )	0.56	0.60
$\Delta I_{in,max}$ ( $R = 300 \Omega$ )	0.95 A	0.84 A

inductor would cause slight current ripple mismatch between the experiment and the analyses.

The conduction losses and switching losses of both active and passive components are estimated according to the experiment data and the parasitic parameters offered in Table I. Due to ZCS operation, the switching losses are minimized. The conduction loss dominates in the total conversion losses. Both the quiescent and dynamic losses of each IC are also estimated according to the provided corresponding data sheet. The estimated losses of individual component are listed in Table III, under 200- $\Omega$

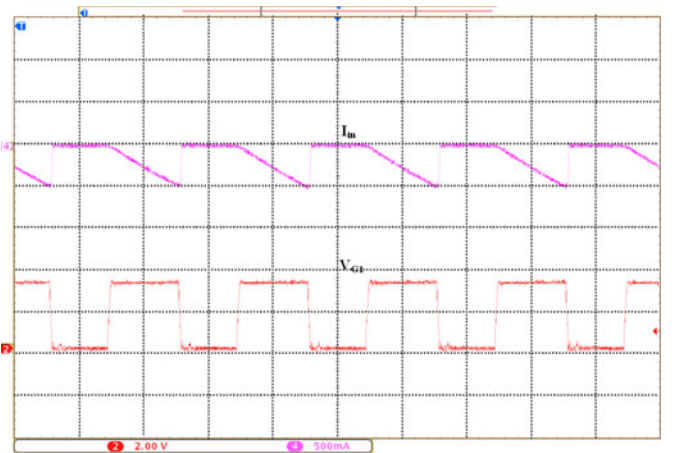


Fig. 17. From top to bottom: oscillograms of input current (1 A/div), buck-boost gate pulse (2 V/div); time 10  $\mu$ s/div,  $R = 300 \Omega$ .

resistive load condition. A 71% conversion efficiency is measured from experiment, which is higher than the state of the art rectifiers for low-voltage applications (61% in [10]).



TABLE III  
LOSS CALCULATION

Category	Component	Estimated Loss
Topology	Inductor	5.7 mW
	Filter Capacitor	0.06 mW
	MOSFETs	5.6 mW
	Diodes	6.3 mW
Controller	Mega 16A	1.98 mW
Sign	Voltage Reference	0.33 mW
Detector	OP-AMP	0.08 mW
Others	Trace and Contact resistances	2.0 mW
Total Loss		22.05 mW

## VII. CONCLUSION

A single stage ac–dc topology for low-voltage low-power energy harvesting applications is proposed in this paper. The topology uniquely combines a boost converter and a buck-boost converter to condition the positive input cycles and negative input cycles, respectively. Only one inductor and one filter capacitor are required in this topology. A compact 2 cm × 2 cm, 3.34-g prototype is fabricated and tested at 54.5 mW. This prototype successfully boosts the 0.4-V, 100-Hz ac to 3.3-V dc. Output voltage is tightly regulated at 3.3 V through closed-loop voltage control. The measured conversion efficiency is 71% at 54.5 mW. In comparison to state-of-the-art low-voltage bridgeless rectifiers, this study employs the minimum number of passive energy storage components, and achieves the maximum conversion efficiency. The future research will be focused on investigating and designing integrated three-phase power electronic interfaces for electromagnetic energy harvesting.

## REFERENCES

- [1] S. Roundy, P. K. Wright, and J. Rabaey, "A study of low level vibrations as a power source for wireless sensor nodes," *Comput. Commun.*, vol. 26, no. 11, pp. 1131–1144, Jul. 2003.
- [2] M. El-hami, P. Glynn-Jones, N. M. White, M. Hill, S. Beeby, E. James, A. D. Brown, and J. N. Ross, "Design and fabrication of a new vibration-based electromechanical power generator," *Sens. Actuators A: Phys.*, vol. 92, no. 1–3, pp. 335–342, Aug. 2001.
- [3] S. P. Beeby, R. N. Torah, M. J. Tudor, P. Glynn-Jones, T. O'Donnell, C. R. Saha, and S. Roy, "A micro electromagnetic generator for vibration energy harvesting," *J. Micromech. Microeng.*, vol. 17, no. 7, pp. 1257–1265, Jul. 2007.
- [4] R. Vullers, R. van Schaijk, and I. Doms, "Micropower energy harvesting," *Solid-State Electron.*, vol. 53, no. 7, pp. 684–693, Jul. 2009.
- [5] C. B. Williams, C. Shearwood, M. A. Harradine, P. H. Mellor, T. S. Birch, and R. B. Yates, "Development of an electromagnetic micro-generator," *IEEE Proc. Circuits Devices Syst.*, vol. 148, no. 6, pp. 337–342, Jun. 2001.
- [6] G. D. Szarka, B. H. Stark, and S. G. Burrow, "Review of power conditioning for kinetic energy harvesting systems," *IEEE Trans. Power Electron.*, vol. 27, no. 2, pp. 803–815, Feb. 2012.
- [7] S. G. Burrow and L. R. Clare, "Open-loop power conditioning for vibration energy harvesters," *Electron. Lett.*, vol. 45, no. 19, pp. 999–1000, Sep. 2009.
- [8] A. Cammarano, S. G. Burrow, D. A. W. Barton, A. Carrella, and L. R. Clare, "Tuning a resonant energy harvester using a generalized electrical load," *Smart Mater. Structures*, vol. 19, no. 5, pp. 1–7, May 2010.
- [9] S. Cheng, N. Wang, and D. P. Arnold, "Modeling of magnetic vibrational energy harvesters using equivalent circuit representations," *J. Micromech. Microeng.*, vol. 17, no. 11, pp. 2328–2335, Nov. 2007.
- [10] R. Dayal and L. Parsa, "A new single stage AC-DC converter for low voltage electromagnetic energy harvesting," in *Proc. IEEE Energy Convers. Congr. Expo.*, Atlanta, GA, USA, Sep. 2010, pp. 4447–4452.
- [11] P. D. Mitcheson, T. C. Green, and E. M. Yeatman, "Power processing circuits for electromagnetic, electrostatic and piezoelectric inertial energy scavengers," *Microsyst. Technol.*, vol. 13, no. 11–12, pp. 1629–1635, Jan. 2007.
- [12] X. Cao, W.-J. Chiang, Y.-C. King, and Y.-K. Lee, "Electromagnetic energy harvesting circuit with feedforward and feedback DC–DC PWM boost converter for vibration power generator system," *IEEE Trans. Power Electron.*, vol. 22, no. 2, pp. 679–685, Mar. 2007.
- [13] E. Lefevre, D. Audigier, C. Richard, and D. Guyomar, "Buck-boost converter for sensorless power optimization of piezoelectric energy harvester," *IEEE Trans. Power Electron.*, vol. 22, no. 5, pp. 2018–2025, Sep. 2007.
- [14] A. Harb, "Energy harvesting: State-of-the-art," *Renewable Energy*, vol. 36, no. 10, pp. 2641–2654, Oct. 2011.
- [15] T. Umeda, H. Yoshida, S. Sekine, Y. Fujita, T. Suzuki, and S. Otaka, "A 950 MHz rectifier circuit for sensor networks with 10 m-distance," in *Proc. IEEE Int. Solid-State Circuits Conf., Digest Tech. Papers*, San Francisco, CA, USA, Feb. 2005, pp. 35–41.
- [16] Y.-H. Lam, W.-H. Ki, and C.-Y. Tsui, "Integrated low-loss CMOS active rectifier for wirelessly powered devices," *IEEE Trans. Circuits Syst. II: Express Briefs*, vol. 53, no. 12, pp. 1378–1382, Dec. 2006.
- [17] C. Peters, J. Handwerker, D. Maurath, and Y. Manoli, "A sub-500 mV highly efficient active rectifier for energy harvesting applications," *IEEE Trans. Circuits Syst. I: Regular Papers*, vol. 58, no. 7, pp. 1542–1550, Jul. 2011.
- [18] T. T. Le, J. Han, A. V. Jouanne, K. Mayaram, and T. S. Fiez, "Piezoelectric micro-power generation interface circuits," *IEEE J. Solid-State Circuits*, vol. 41, no. 6, pp. 1411–1420, Jun. 2006.
- [19] Y. Rao and D. P. Arnold, "An input-powered vibrational energy harvesting interface circuit with zero standby power," *IEEE Trans. Power Electron.*, vol. 26, no. 12, pp. 3524–3533, Dec. 2011.
- [20] S. Cheng, R. Sathe, R. D. Natarajan, and D. P. Arnold, "A voltage-multiplying self-powered AC/DC converter with 0.35-V minimum input voltage for energy harvesting applications," *IEEE Trans. Power Electron.*, vol. 26, no. 9, pp. 2542–2549, Sep. 2011.
- [21] S. Cheng, Y. Jin, Y. Rao, and D. P. Arnold, "An active voltage doubling AC/DC converter for low-voltage energy harvesting applications," *IEEE Trans. Power Electron.*, vol. 26, no. 8, pp. 2258–2265, Aug. 2011.
- [22] R. Moghe, D. Divan, and F. Lambert, "Powering low-cost utility sensors using energy harvesting," in *Proc. 14th Eur. Conf. Power Electron. Appl.*, Birmingham, U.K., Aug. 2011, pp. 1–10.
- [23] T. J. Kazmierski, B. M. A. Hashimi, S. P. Beeby, and R. N. Torah, "An integrated approach to energy harvester modeling and performance optimization," in *Proc. IEEE Int. Behavioral Model. Simul. Workshop*, San Jose, CA, USA, Sep. 2007, pp. 121–125.
- [24] P. D. Mitcheson, T. C. Green, and E. M. Yeatman, "Power processing circuits for MEMS inertial energy scavengers," in *Proc. Des., Test, Integr. Packag. MEMS/ MOEMS*, Stresa, Italy, Apr. 2006, pp. 1629–1635.
- [25] D. Kwon and G. A. Rincon-Mora, "A rectifier-free piezoelectric energy harvester circuit," in *Proc. IEEE Int. Symp. Circuits Syst.*, Taipei, Taiwan, Jun. 2009, pp. 1085–1088.



**Haoyu Wang** (S'12) received the B.S.E. degree (with Highest Hons.) in electrical engineering from Zhejiang University, Hangzhou, China, in 2009. He is currently working toward the Ph.D. degree in the Department of Electrical and Computer Engineering, University of Maryland, College Park, MD, USA.

He was an Intern with GeneSIC Semiconductor, Inc., in summer 2012. His research includes analog and radio frequency integrated circuits design, power electronics interface design for human motion energy harvesting, SiC-based power electronic converters, as well as plug-in hybrid electrical vehicles.





**Yichao Tang** (S'12) received the B.S. degree from Shanghai Jiaotong University, Shanghai, China, in 2009, and the M.S. degree from Illinois Institute of Technology, Chicago, IL, USA, in 2011 both in electrical engineering. He is currently working toward the Ph.D. degree in the Department of Electrical and Computer Engineering, University of Maryland, College Park, MD, USA.

His research interests include modeling, analysis and design of power electronic-based biomechanical energy harvesting systems, ultracompact high-voltage power drive interfaces for electroactive polymer actuators-based micro-robotic insects, as well as power conditioning systems for sea-based electric vehicles.



**Alireza Khaligh** (S'04–M'06–SM'09) is an Assistant Professor and The Director of Power Electronics, Energy Harvesting and Renewable Energies Laboratory at the Department of Electrical and Computer Engineering, and the Institute for Systems Research at the University of Maryland, College Park (UMCP), USA. Prior to UMCP, he was a Postdoctoral Research Associate in the Grainger Center for Electric Machinery and Electromechanics, University of Illinois at Urbana-Champaign, Urbana, IL, USA, and also an Assistant Professor at Illinois Institute of Tech-

nology (IIT), Chicago, IL, USA. He is an author/coauthor of more than 100 journal and conference papers. His major research interests include modeling, analysis, design, and control of power electronic converters, electric and plug-in hybrid electric vehicles, biomechanical energy harvesting, and miniaturized power electronic interfaces for microrobotic applications.

Dr. Khaligh is the recipient of the Best Vehicular Electronics Paper Award from the IEEE Vehicular Technology Society (2012), the Ralph R. Teetor Educational Award from the Society of Automotive Engineers (2010), the Armour College of Engineering Excellence in Teaching Award from IIT (2009), and the Distinguished Undergraduate Student Award from the Sharif University of Technology (1999). He is the General Chair of the 2013 IEEE Transportation Electrification Conference and Exposition, and the Grants and Awards Chair for the 2013 IEEE Applied Power Electronics Conference and Exposition. He was the Program Chair of the 2011 IEEE Vehicle Power and Propulsion Conference, and the Program Co-Chair of the 2012 IEEE Transportation Electrification Conference and Exposition. He is an Associate Editor of the IEEE TRANSACTIONS ON VEHICULAR TECHNOLOGY (TVT), and a Guest Associate Editor for the Special Issue of the IEEE TRANSACTIONS ON POWER ELECTRONICS ON TRANSPORTATION ELECTRIFICATION AND VEHICLE SYSTEMS. He was a Guest Editor for the Special Section of the IEEE TVT on Sustainable Transportation Systems, and a Guest Editor for the Special Section of the IEEE TRANSACTIONS ON INDUSTRIAL ELECTRONICS ON ENERGY HARVESTING.